

Journal of Materials Chemistry A

Accepted Manuscript



This is an *Accepted Manuscript*, which has been through the Royal Society of Chemistry peer review process and has been accepted for publication.

Accepted Manuscripts are published online shortly after acceptance, before technical editing, formatting and proof reading. Using this free service, authors can make their results available to the community, in citable form, before we publish the edited article. We will replace this *Accepted Manuscript* with the edited and formatted *Advance Article* as soon as it is available.

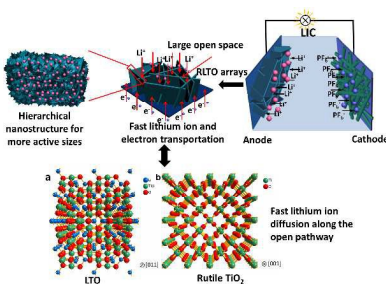
You can find more information about *Accepted Manuscripts* in the [Information for Authors](#).

Please note that technical editing may introduce minor changes to the text and/or graphics, which may alter content. The journal's standard [Terms & Conditions](#) and the [Ethical guidelines](#) still apply. In no event shall the Royal Society of Chemistry be held responsible for any errors or omissions in this *Accepted Manuscript* or any consequences arising from the use of any information it contains.

Rutile-TiO₂ Decorated Li₄Ti₅O₁₂ Nanosheet Arrays with 3D Interconnected
Architecture as Anode for High Performance Hybrid Supercapacitor

Authors: Lin Gao, Dekang Huang, Yan Shen, Mingkui Wang*

Hybrid Supercapacitor exhibits an ultrahigh energy density of 74.85 Wh kg⁻¹ at a power density of 300 W kg⁻¹.





Journal Name

ARTICLE

Rutile-TiO₂ Decorated Li₄Ti₅O₁₂ Nanosheet Arrays with 3D Interconnected Architecture as Anode for High Performance Hybrid Supercapacitor

Received 00th January 20xx,
Accepted 00th January 20xx

Lin Gao, Dekang Huang, Yan Shen, Mingkui Wang*

DOI: 10.1039/x0xx00000x

www.rsc.org/residual

Herein, we report on the rutile TiO₂ decorated hierarchical Li₄Ti₅O₁₂ nanosheet arrays for lithium ion hybrid supercapacitor application for the first time. It is noted that the self-supported arrays manifest impressive rate capability and cycling stability, showing a reversible specific capacity of 142.9 mAh g⁻¹, and maintaining 92.3% of its initial capacity over 3000 cycles at a rate of 30 C. Lithium ion hybrid supercapacitor, constructed with Li₄Ti₅O₁₂ nanosheet arrays and nitrogen doped carbon nanotubes (N-CNTs), exhibits an ultrahigh energy density of 74.85 Wh kg⁻¹ at a power density of 300 W kg⁻¹. The self-supported Li₄Ti₅O₁₂-rutile TiO₂ nanosheet arrays with hierarchical 3D interconnected nanostructure, as well as the efficient lithium diffusion along the [011] direction for Li₄Ti₅O₁₂ and [001] for rutile TiO₂, play important role in the outstanding energy storage performance.

1. Introduction

Lightweight and high power density capacitors are of particular interest for the development of hybrid and electric vehicles as well as portable electronics. The fast-charging devices allow for significant energy saving, because they can accumulate energy during braking and release it during acceleration. However, the conventional supercapacitors (SCs) individuals can be unable to meet the ever-growing requirements for devices with high energy density.^[1-3] It is commonly recognized that the SCs are capable of delivering power density as high as 10 kW kg⁻¹ with long cycle life (>100,000 cycles), however, they are constrained by the poor energy density (5~10 Wh kg⁻¹).^[4,5] Accordingly, lithium ion batteries (LIBs) possess high energy density (150~200 Wh kg⁻¹), but suffer from the limited cycle life (<1000 cycles) and low power density (<1000 W kg⁻¹). A new strategy noted as lithium ion hybrid electrochemical supercapacitors (LICs), which consist of a capacitor-type cathode (mainly carbon materials), a lithium ion battery-type anode, and organic electrolyte, has attracted worldwide attention with high energy density while preserving high power density. It is expected that the advantages of LIBs and SCs could be combined in LICs.^[6] Nevertheless, the imbalance of the reaction kinetics between the two electrodes have become one of the most important challenges. The sluggish solid-state ion diffusion in the bulk anodes, especially at a high current density, drastically retards the LICs' performance.^[7] The anodes with open nanostructure in the hybrid supercapacitor would be benefited with ion diffusion. Also excellent electronic and ionic conductivity, the intimate

adhesion with the current collector as well as ultrahigh electrochemical stability should be possessed for these anodes.

Recently, nanostructured materials including Fe₂O₃,^[5] VN,^[8] TiNb₂O₇,^[4] Si,^[9] MnO,^[7] TiO₂^[6,10,11], and Li₄Ti₅O₁₂^[2,12-15], have been exploited as anode for LICs and shown impressive electrochemical performance. Amongst them, titanium based compounds are the most appealing materials due to the specified lithium-insertion-type reaction.^[1,10] For instance, a carbon nanotube cathode and a TiO₂ (B) nanowire anode have been developed to LICs by Wang *et al.*,^[6] delivering an energy density of 12.5 Wh kg⁻¹ at a rate of 10 C with excellent cycling performance. Mesoporous TiO₂ microspheres were introduced to assemble the LIC along with activated carbon as cathode,^[16] which achieved an energy density of 79.3 Wh kg⁻¹ at a power density of 178.1 W kg⁻¹, retaining 98% of the initial energy density after 1000 cycles. It is noted that the nanostructured TiO₂ allows for easy penetration of electrolytes into the active materials, and thereby advances lithium ion diffusion and rate performance. Meanwhile, the kinetics mismatch between cathode and anode in LICs can be significantly circumvented. Carbon-nanotube-threaded TiO₂ nanocrystals with 3D spherical architecture were subsequently realized by Chen *et al.*,^[11] delivering an energy density of 22.3 Wh kg⁻¹ at a power density of 13.9 kW kg⁻¹. The excellent performance can be attributed to the versatile engineering of nanostructured TiO₂ on conductive carbon nanotubes, which enhances the electric conductivity along with lithium ion diffusion, and thereafter guarantees an ideal rate performance. Spinel structured Li₄Ti₅O₁₂ (LTO) as the zero strain lithium insertion type electrode, with salient advantages of impressive cycling performance, safety in operation, environmental friendliness, and thermodynamically flat charge-discharge plateau as well, have also aroused intensive attention.^[17-20] However the low electronic conductivity and lithium ion diffusion coefficient for LTO are still main issues to impede its practical implementation.^[21] The commonly used protocols to improve this

Wuhan National Laboratory for Optoelectronics, Huazhong University of Science and Technology, Luoyu Road 1037, Wuhan 430074, P. R. China.
E-mail: mingkui.wang@mail.hust.edu.cn
Electronic Supplementary Information (ESI) See DOI: 10.1039/x0xx00000x

performance are mainly focused on structure engineering LTO particles, in combination with decorating the LTO with secondary conductive materials, such as carbon and conductive polymers.^[1] For example, carbon coated LTO particles have been initiated to constitute the LICs,^[15] whose lithium ion diffusion coefficient and electronic conductivity are greatly enhanced. The resulted LICs have shown excellent electrochemical performance with 95% of its initial capacity retained after 1000 cycles. Nanocrystalline LTO attached on carbon fibre nanocomposite^[14] and graphene-wrapped^[12] LTO have also been developed as anode for LICs with enhanced energy and power density. The abovementioned titanium based materials for LICs must be mixed with insulating binder, followed by being coated on current collector. The weak adhesion between the active materials and the substrate determines the slow lithium ion and electron transportation in these devices.^[22,23] Therefore, it is highly desirable to improve lithium ions and electrons transportation for the anode materials in LICs.

This work presents a hybrid capacitor using rutile TiO₂ decorated LTO (denoted as RLTO) with 3D interconnected nanostructure as negative electrode. The unique hierarchical nanosheet construction with interconnected 3D open microstructure allows for the robust penetration of electrolytes into the active materials and shows up the enhanced rate capability for RLTO electrode. The exposed (011) facets for LTO and (001) facets for rutile TiO₂ provide fast diffusion pathways for lithium ions. The self-supported RLTO nanosheet arrays possess lithium ion diffusion coefficient as high as $5.83 \times 10^{-10} \text{ cm}^2 \text{ s}^{-1}$. This guarantees a direct assembly of electronic devices without any polymeric binder, and thus, an enhanced energy and power density. The cathodes in the hybrid supercapacitor are generally carbon-based materials, which should possess properties of high electrical conductivity and large specific surface area. Porous nitrogen doped carbon nanotubes (N-CNTs) are selected as the cathode due to high electrical conductivity and large specific surface area.^[24]

2. Experimental section

Preparation of RLTO nanosheet arrays and N-CNTs: TiO₂ nanosheet arrays were fabricated based on our previous work.^[25,26] Firstly, Ti foils (50×30×0.1 mm³ purity≥99.99%) were ultrasonically cleaned by ethanol and acetone for 10 min, respectively. Then the dried Ti foils were placed against the wall of Teflon-lined autoclave (90 mL) which contains 1 M NaOH solution with volume of 40 mL followed by being held at 180 °C for 12 h in the oven. The obtained film was immersed in the diluted HCl solution (0.3 M) for 2 h to thoroughly exchange the Na⁺ with H⁺ and rinsed with distilled water to clean up the residual. The resultant film is denoted as H₂Ti₂O₅·H₂O nanosheet arrays, which is directly calcined in air at 500 °C for 1 h to prepare TiO₂ nanosheet arrays. Simultaneously, the obtained H₂Ti₂O₅·H₂O nanosheet arrays were placed in the solution of LiOH·H₂O (2 M) at 60 °C for 10 h, followed by being carefully rinsed by the ethanol and calcined in N₂ at 600 °C for 3 h, thus RLTO nanosheet arrays are finally obtained. On the other hand, the nitrogen doped carbon nanotubes (N-CNTs) are realized according to the previous reports.^[24] FeCl₃·6H₂O (14.4 mM) and mmethyl orange (2.4 mM) as the template were dissolved in the deionized water (480 mL), then pyrrole (0.84 mL) was stepwise added to the

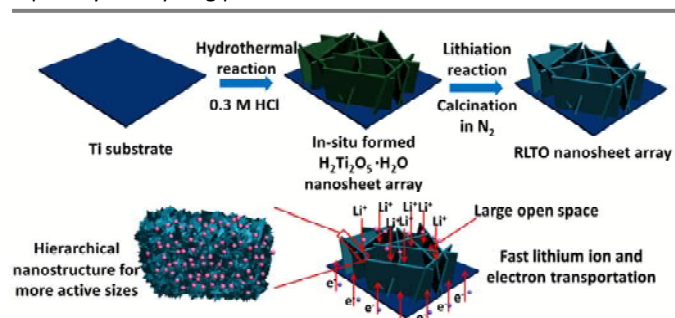
aboved solution and held stirring for 24 h at the room temperature. The precipitate was filtered and washed thoroughly with deionized water and ethanol until the solution became colorless. Through the vacuum freeze drying process, the obtained polypyrrole nanotubes were carbonized in N₂ at 800 °C for 2 h, followed by the uniform mixing with KOH according to the mass ratio of 1:4 and being calcined in N₂ at 700 °C for 1 h. Consequently, the resulted powder was rinsed with a large amount of HCl (1 M) and deionized water for three times followed by the drying at 60 °C for 12 h and the N-CNTs were obtained.

Material characterizations: Field-emission scanning electron microscopy (FESEM, Nova Nano SEM 450, Netherlands) measurement was performed to observe the morphologies of our synthesized materials. The porous structure and lattice fringes were further determined utilizing Transmission electron microscopy (TEM, Tecnai G220) operation. All of the phases for as-prepared arrays were analyzed utilizing X-ray diffraction (XRD) characterization using X' Pert PRO (PANalytical B.V., Netherlands) diffractometer with Cu Kα1 irradiation ($\lambda=1.5406 \text{ \AA}$). The nitrogen doping for N-CNTs was determined by X-ray photoelectron spectroscopy (XPS, AXIS-ULTRA DLD-600W, Shimduzu) measurement, and the mean pore size distribution in combination with specific Brunauer-Emmett-Teller (BET) surface area of N-CNTs was obtained by N₂ isotherm adsorption/desorption measurement using ASAP 2020 (Micromeritics). We first weighted a piece of circular slice (1.13 cm²) with an electronic balance (METTLER TOLEDO, XS3DU, Switzerland d=0.001 mg). The bare slice was weighted again after polishing away the active materials on the Ti substrate with abrasive paper. Therefore, the weight of the active materials on the Ti substrate (0.2~0.3 mg cm⁻²) could be precisely determined.

Device performance measurements: The resultant TiO₂ and RLTO films were punched to the wafer with diameter of 12 mm and directly assembled to 2016 half cells using porous polypropylene membrane as a separator. The TiO₂ and RLTO arrays were utilized as the working electrode without any additive conductors and polymeric binder, while the corresponding Li metal foils were utilized as the counter and reference electrodes. The N-CNTs were mixed with polyvinylidene fluoride (PVDF) and carbon black as the mass ratio of 8:1:1, dissolved into the N-methylpyrrolidone (NMP) solvent and stirred for 12 h at ambient temperature, which was coated on the Al foil and dried at 80 °C for 12 h in *vacuo*. The obtained films were punched to the wafer (12 mm) and assembled to 2016 half cells, on the other side, the LICs were assembled with N-CNTs as the cathode and RLTO arrays as the anode. The device fabrication was carried out in an Ar-filled glove-box, in which the water and oxygen content were remained less than 1 ppm. The composition of electrolytes is LiPF₆ (1 M) dissolved in a mixture of ethylene carbonate (EC), ethylmethyl carbonate (EMC) and dimethyl carbonate (DMC) with a volume ratio of 1:1:1. The electrochemical performance of our prepared electrodes was performed using Land (CT 2001A Wuhan, China) battery system with the voltage window of 1~3 V (vs. Li⁺/Li) at various current densities. Cyclic voltammetry (CV) and electrochemical impedance spectroscopy (EIS) measurements were conducted using a CHI 660D electrochemical workstation.

3. Results and discussions

Scheme 1 depicts the overall synthesis process of RLTO nanosheet arrays. The RLTO nanosheet arrays were finally derived with the $\text{H}_2\text{Ti}_2\text{O}_5 \cdot \text{H}_2\text{O}$ as the precursor, followed by chemical lithiation and calcination in N_2 (see XRD result and SEM image in Figure S1a and b)^[11]. It is worth noting, that the hierarchical 3D interconnected nanosheet architecture provides open channels and more active sizes for the facile lithium ion diffusion. The self-supported arrays possesses faster lithium ion and electron transportation compared to the conventional electrode derived from coating method using polymeric binder, substantially guarantees the excellent rate capability and cycling performance.



Scheme 1 Schematic illustration of the LTO nanosheet arrays.

Figure 1a highlights XRD patterns of RLTO (red line) and TiO_2 (black line) nanosheet arrays. For the TiO_2 nanosheet arrays, all of peaks can be assigned to the anatase TiO_2 besides the typical peaks for Ti. Interestingly, there exists a weak peak at 28.7° from $\text{TiO}_2(\text{B})$.^[25,26] For the RLTO sample, the peaks located at 18.5° , 43.8° and 56.8° can be indexed to cubic spinel $\text{Li}_4\text{Ti}_5\text{O}_{12}$, and the other weak peaks at 27.8° , 53.3° and 63.2° can be indexed to the rutile TiO_2 .^[27] The strong peak intensity demonstrates the RLTO and TiO_2 nanosheet arrays are well-crystallized. Leaf-like TiO_2 and RLTO nanosheets, with $1\sim 2\ \mu\text{m}$ in width as well as open 3D interconnected architecture, are uniformly distributed as shown in Figure 1b and 1c. The LTO arrays inherit the morphology of TiO_2 even through calcination at $600\ ^\circ\text{C}$. Figure 1d presents the SEM image of N-CNTs, in which a large number of nanotubes with length of $2\sim 4\ \mu\text{m}$ are detected and the obvious tubular structure is further determined according to the TEM image (the inset). The corresponding XRD pattern (Figure S2) exhibits broad peaks at 23° and 42.7° , indicating the highly amorphous structure.^[28] In order to determine the nitrogen doping into CNTs, XPS characterization was carried out and the results are shown in Figure S3a, in which three distinct peaks are assigned to C, N and O elements.^[29] The N1s spectrum (Figure S3b) deconvoluted into three peaks at 398.8 eV, 400.6 eV and 401.9 eV, are indexed to pyridinic (N-6), pyrrolic/pyridine (N-5) and quaternary (N-Q) nitrogen,^[30,31] suggesting the nitrogen doping for CNTs. The mass fractions of C, N, O was calculated to be approximately 93.26%, 3.22% and 3.52%, respectively. N_2 absorption-desorption measurement was carried out to determine the specific surface area of N-CNTs and pore size distribution. A large specific surface area of $2236.5\ \text{m}^2\ \text{g}^{-1}$ is obtained with pore volume of $1.8\ \text{cm}^3\ \text{g}^{-1}$ (Figure S4). The mean pore size distribution can be detected at 2.0 and 3.5 nm using the Barrett-Joyner-Halenda (BJH) method. It is noted that the ultrahigh surface area as well as these mesoporosity are beneficial to the transportation of ions, thus providing abundant active sizes for ion accumulation.^[31]

Representative TEM images of TiO_2 and RLTO arrays are introduced in Figure 2 to further analyze the nanostructures. An individual TiO_2 nanosheet with around $3\ \mu\text{m}$ in width and $5\ \mu\text{m}$ in length is observed in the view, which is composed of a large quantity of nanoparticles ($\sim 30\ \text{nm}$) and nanorods ($100\text{-}200\ \text{nm}$), accompanying with a large amount of mesopores around $5\text{-}10\ \text{nm}$ in size uniformly distributed inside the nanosheet (Figure 2a and 2b). Figure 2c shows the corresponding high-resolution TEM (HRTEM) image for anatase TiO_2 with a spacing of $0.35\ \text{nm}$, which

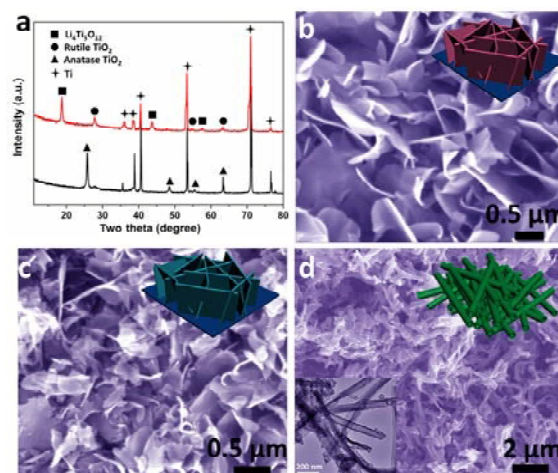


Fig. 1 (a) The XRD patterns for the TiO_2 nanosheet (black line) and RLTO nanosheet arrays (red line) and arrays, SEM images of (b) TiO_2 nanosheet arrays and (c) RLTO nanosheet arrays, (d) SEM image and TEM image (the inset) of N-CNTs.

can be contributed to the typical (101) plane.^[32] Figure 2d-f display the TEM images of RLTO nanosheet arrays obtained from the above mentioned nanostructured $\text{H}_2\text{Ti}_2\text{O}_5 \cdot \text{H}_2\text{O}$. There exist a number of wrinkles and mesopores inside TiO_2 nanosheet which is composed of nanorods ($200\text{-}400\ \text{nm}$ in length) and nanoparticles ($\sim 40\ \text{nm}$) according to the TEM images (Figures 2d, 2e and S5). The substantial nanorods and nanoparticles form the hierarchical and interconnected architecture containing with mesopores, which provides abundant pathways for lithium ion diffusion, thereafter favors the rate capability. The corresponding lattice fringes in Figure 2f shows the typical (111) plane of LTO with an inter-planar distance of $0.48\ \text{nm}$, and the fast Fourier-transform (FFT) pattern in the inset shows the [011] zone axis of LTO with exposed (011) facets.^[33] The spacing of $0.32\ \text{nm}$ is assigned to the (110) plane of rutile TiO_2 , which indicates that rutile TiO_2 are surrounded by exposed (001) facets with high lithium ion diffusion coefficient of $10^{-6}\ \text{cm}^2\ \text{s}^{-1}$ along the [001] direction.^[34] The crystal structure of LTO and rutile TiO_2 are presented in Figure 3 a and b, in which the view direction are [011] and [001] directions for LTO and rutile TiO_2 , respectively. It can be obviously seen that there exist open lithium ion diffusion pathways along the [011] and [001] crystal orientations, which is rather beneficial to the lithium ion transportation for the RLTO composition.

Half cells were assembled for abovementioned RLTO arrays to analyze their electrochemical performance. Indispensably, cyclic voltammetry (CV) curves in Figure 4a are introduced to investigate the redox reaction of the RLTO half cells, in which two pairs of redox peaks located at $1.50\ \text{V}/1.65\ \text{V}$ can be assigned to the lithium/delithium reactions for LTO^[26,35,36] and the three overlapped

redox peaks illustrate the excellent reversibility of RLTO electrode. Notably, there were no redox peaks assigned to the TiO₂ for RLTO electrodes, which may be attributed to the small quantity of the rutile TiO₂ in RLTO composites. What's more, a larger current intensity was observed for the RLTO electrode than that of the TiO₂ electrode (Figure S6a), demonstrating the lower overall resistance,^[22] which can be further verified by electrochemical impedance spectroscopy (EIS) technique. The

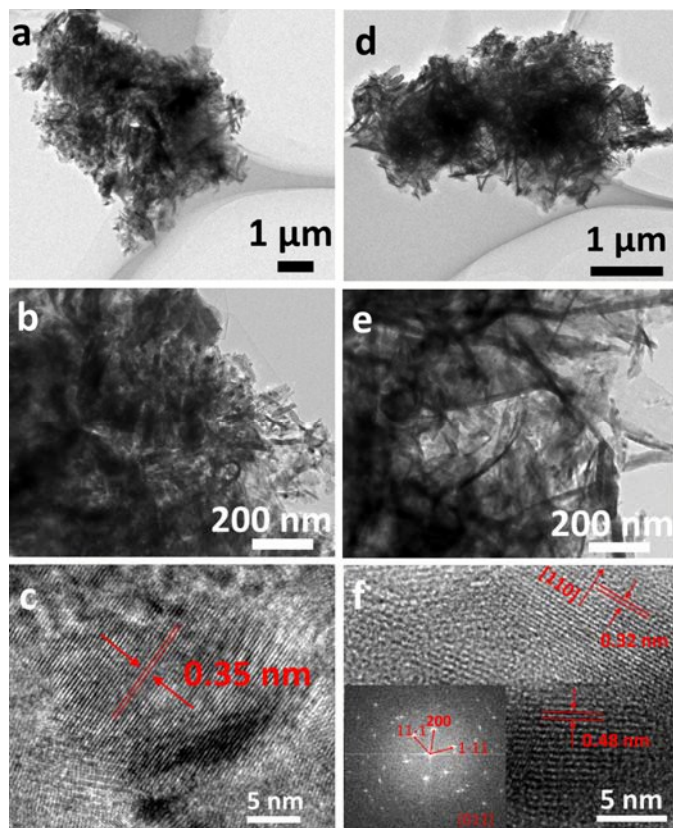


Fig. 2 (a) TEM image, (b) the magnified TEM image, and (c) the corresponding HRTEM image of TiO₂ nanosheet arrays. (d) TEM image, (e) The magnified TEM image, and (f) the corresponding HRTEM image of RLTO nanosheet arrays. The inset shows the FFT pattern.

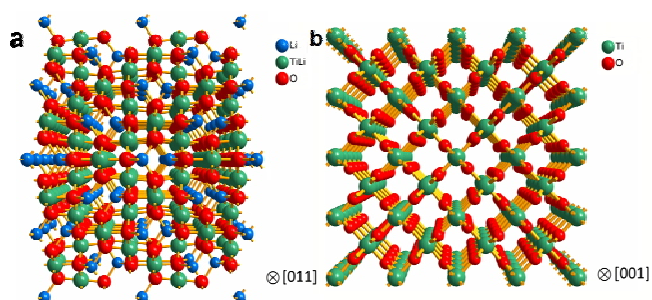


Fig. 3 Crystal structure of (a) LTO along [011] direction and (b) rutile TiO₂ along [001] direction.

Nyquist plots for RLTO electrode after the rate performance operation are given in Figure S6b in the frequency range of 100 kHz to 0.1 Hz, consisting of a pair of semicircles at the medium frequency and inclined lines at the low frequency. For the

comparison purpose, Figure S6b also gives the impedance spectroscopy of the TiO₂ electrode. As the frequency increasing, there are several elements in the equivalent circuit model corresponding to the ionic diffusion in the electrolyte, the charge transfer process at electrode/electrolyte interface, and the charge transport process in the surface film, respectively. An equivalent circuit model (the inset of Figure S6b) was employed to analyze the EIS data, in which R_s is the resistance of the electrolyte, C_{Li} is the capacitance phase element, and R_{ct} represents the charge-transfer resistance at the electrode/electrolyte interface. R_s , R_{sf} and R_{ct} as illustrated in the equivalent circuit represent the series resistance (resistance of the electrolyte, separator and electrodes), the contact resistance for the surface film between electrolyte and electrode, and the charge-transfer resistance, respectively.^[37] For better fitting, all capacitor elements were replaced by constant phase element (CPE) exponent p quite close to the perfect capacitor values, $p \approx 1$.^[38-40] The charge-transfer resistance (R_{ct}) is the major influence to the overall resistance of the electrode,^[41] which is evaluated to be 81.7 and 210.1 Ω for the RLTO and TiO₂ electrodes, respectively. The corresponding lithium ion diffusion coefficients are calculated to be $5.83 \times 10^{-10} \text{ cm}^2 \text{ s}^{-1}$ and $2.53 \times 10^{-10} \text{ cm}^2 \text{ s}^{-1}$ for RLTO and TiO₂ electrodes according to the following equations (1) and (2):^[42]

$$D_{Li} = \frac{(RT)^2}{2(A n^2 F^2 C_{Li} \sigma)^2} \quad (1)$$

$$Z_{re} = R_{ct} + R_s + \sigma \omega^{-0.5} \quad (2)$$

where R represents the gas constant, F represents the Faraday's constant, A denotes the area of the electrode and C_{Li} denotes the molar concentration of lithium ions. The value of σ is calculated on the basis of the slopes shown in Figure S7. The above results demonstrate that the unique RLTO nanosheet arrays have competitive electronic conductivity and lithium ion diffusion, further proving that the special 3D architecture and crystal structure gives rise to the rate performance. The galvanostatic charge-discharge curves are available in Figure 4b for the RLTO electrode, in which a wide charge-discharge plateau around 1.55 V can be obviously detected and is identical with the typical CV curve of LTO.^[43] No obvious plateau for TiO₂ and no distinct potential polarization are detected for the RLTO electrode at various rates. In contrast, polarization is highly serious for the TiO₂ electrode as the current density changes from 1C to 30 C (Figure S6c).

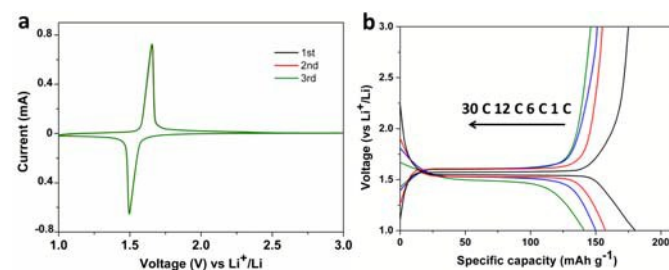


Fig. 4 (a) CV curves of RLTO electrode at a scan rate of 0.5 mV s^{-1} . (b) The galvanostatic charge-discharge curves in the voltage window of 1-3 V at different current densities for the RLTO electrode.

The rate performance of the RLTO electrode at current densities of 1 C, 6 C, 12 C, 30 C, and back to 1 C (1 C=170 mA g⁻¹) was further characterized and the results are shown in Figure 5a. Although the initial discharge capacity at 1 C for RLTO electrode is merely 185.0 mAh g⁻¹, the capacity degradation for RLTO electrode is much alleviated in comparison with the TiO₂ electrode upon the increasing current density. Even at a current density as high as 30 C, there is still a specific capacity of 142.9 mAh g⁻¹ for the RLTO electrode, being higher than the capacity of 114.4 mAh g⁻¹ for the TiO₂ electrode. After the rate is returned to 1 C, the reversible capacity of 173.7 mAh g⁻¹ for RLTO electrode can be remained, close to the theoretical capacity of this material. Figure 5b presents the cycling performance for RLTO electrode at a rate of 1 C. Interestingly the discharge capacity increases to 183.6 mAh g⁻¹ during the 130 cycle testing at a rate of 1 C. In order to further examine the cycling performance of RLTO nanosheet arrays, a test of 3000 cycles was performed at an ultrahigh current density (*i.e.*, 30 C). As seen from Figure 5c, the RLTO electrode exhibits impressive stability. A specific capacity of 132.3 mAh g⁻¹ can be maintained through an extended cycling test at a fast charge-discharge condition, being 92.3% of its initial capacity. The corresponding coulombic efficiency is close to 100%. It is worth noting that the RLTO nanosheet structure after 3000 cycles at 30 C have no obvious change and aggregation compared with the original morphology (Figure 5d, e), showing sturdy hierarchical construction with interconnected architecture. This is significantly important for the cycling stability especially at high current densities. Figure 5f compares the rate capability between the self-supported LTO nanosheet arrays and the previously reported LTO-based electrodes, including LTO hollow spheres,^[44] LTO microspheres,^[45,46] LTO-TiO₂ nanocomposite,^[42,47,50] LTO-TiO₂ nanosheets,^[26,27,37] flexible LTO-CNTs composite,^[43] LTO-graphene nanocomposite^[48] as well as LTO-CNTs-graphene nanocomposite.^[49] It is remarkably demonstrated that the self-supported hierarchical RLTO electrode shows the most excellent rate capability. This will benefit the electrochemical performance of LICs as discussion below. The excellent electrochemical properties can be attributed to the following aspects: (1) A special hierarchical nanosheet construction with interconnected 3D open microstructure, with the macropores around 1 μm constructed by the interconnected nanosheets and served as the reservoirs for electrolytes, and the mesopores around 5-10 nm inside nanosheets provided as accessible channels for lithium ions, allows for the robust penetration of electrolytes into the active materials and advances rate capability; (2) The intimate adhesion between the active materials and substrate plays important role in facilitating electron and ion transportation; (3) The interconnected 3D architecture with large open space imparts the RLTO arrays with structural integrity, which can effectively hinder the aggregation during fast charge-discharge process; (4) The exposed (011) facets for LTO and (001) facets for rutile TiO₂ in RLTO composite provide efficient lithium diffusion channels and largely improve the lithium ion diffusion coefficient.

Hybrid supercapacitor was assembled by utilization of the self-supported RLTO arrays as anode and N-CNTs as cathode. The scheme in Figure 6a illustrates Li⁺ ions intercalate into the anode and the PF₆⁻ ions accumulate on the surface of cathode electrode

during the charge process. In the discharge process, the Li⁺ ions and PF₆⁻ return back to the electrolyte. The mass loading was optimized to be 1:3 with respect to anode and cathode materials. Figure S8 shows the CV curves of RLTO//N-CNTs (0.5-2.5 V) hybrid supercapacitor, RLTO (1-3 V) and CNTs half (3-4.5 V) cells at a scan rate of 5 mV s⁻¹. For the hybrid supercapacitor, the capacitive and redox reactions are observed in the meantime. Compared to the RLTO half cell, the overpotential is greatly alleviated for LICs with the capacitor-type cathode and lithium ion battery-type anode.

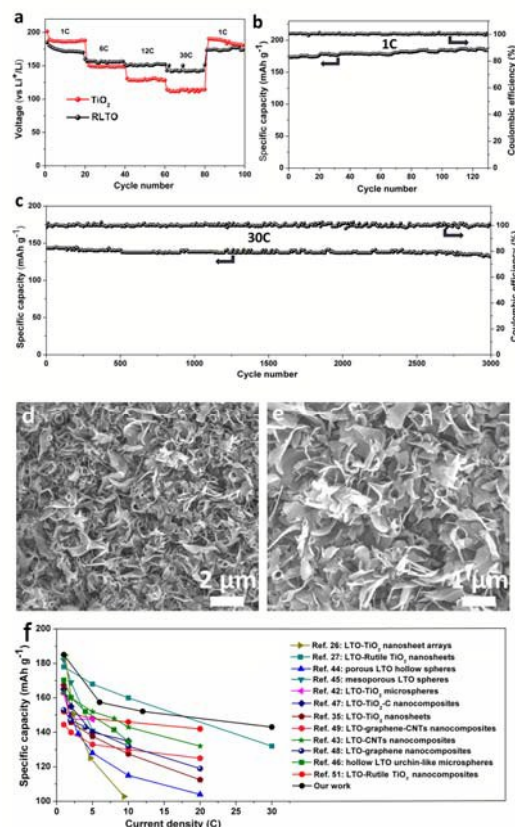


Fig. 5 (a) Rate performance of the RLTO and TiO₂ electrodes. The cycling performance of the RLTO electrode at (b) 1C and (c) 30 C. Right ordinate is the corresponding coulombic efficiency. (d, e) SEM images of RLTO nanosheet arrays after 3000 cycles at 30 C. (f) Comparison of the rate performance the RLTO nanosheet arrays in this study to previously reported RLTO-based anode materials.

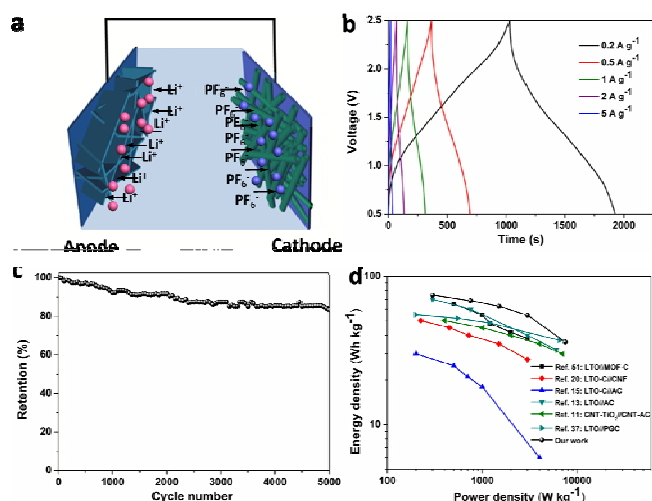


Fig. 6 (a) schematic illustration of LICs with RLTO nanosheet arrays as anode and N-CNTs as cathode, (b) Galvanostatic charge-discharge curves of LICs at different current densities, (c) The capacity retention of LICs over 5000 cycles, (d) Ragone plots of the RLTO//N-CNTs hybrid supercapacitor in this study with other previously reported LICs.

This is caused by the synergetic effect between anode and cathode for LICs.^[51] The Galvanostatic charge-discharge curves at applied current densities of 0.2 A g^{-1} , 0.5 A g^{-1} , 1 A g^{-1} , 2 A g^{-1} and 5 A g^{-1} for LICs with the potential window of 0.5–2.5 V are displayed in Figure 6b. The current density was calculated on the basis of the total mass for the cathode and anode. It is noted that charge-discharge curves exhibit a gradually sloping profile in the range of 1–2 V different from the linear curves, which can be attributed to the Faradic reaction for RLTO and is beneficial to the energy density. The unobvious voltage plateau around 1.5 V for RLTO may result from the special electrochemical property of LICs which is the combination of LIBs and SCs. Meanwhile, the LIC shows ultra-long cycling performance, remaining 83.3% of its initial capacity after 5000 cycles at 2 A g^{-1} as shown in Figure 6c. The corresponding specific energy density and power density are calculated according to the following equations:

$$P = (V_{\max} + V_{\min}) \times i / 2m \quad (3)$$

$$E = P \times t / m \quad (4)$$

V_{\max} and V_{\min} are the highest and lowest potential in the charge-discharge process for hybrid devices. The hybrid supercapacitor possesses the maximum energy density of 74.85 Wh kg^{-1} at a power density of 300 W kg^{-1} . An energy density of 36.04 Wh kg^{-1} can be still achieved even at a high power density of 7500 W kg^{-1} . Figure 6d shows the Ragone plots of specific energy density and power density for the prepared RLTO//CNTs electrode combined with other previous reports, including LTO//porous carbon with graphitic shells,^[37] TiO_2 //CNTs-AC,^[11] LTO//AC,^[13] C-LTO//AC,^[15] C-LTO//CNF^[20], and LTO//MOF-C^[52]. The perfect synergetic effect between RLTO nanosheet arrays and CNTs, by which the ultrafast lithium/delithium reaction on the RLTO anode because of the special hierarchical nanostructure and unique crystal structure matches well with the capacitor-type N-CNTs cathode, could be the major factor to determine the excellent rate and stability

performance of the hybrid device. Even so, the further optimization for the performance of LICs is still needed.

4. Conclusions

In summary, N-CNTs and hierarchical RLTO nanosheet arrays with 3D interconnected architecture have been successfully fabricated. From the aspect of morphology, the hierarchical 3D open interconnected structure for RLTO nanosheet arrays provides open channels for lithium ions and electrons as well as effectively mitigates the aggregation because of the stable interconnected construction. From the aspect of crystal structure, the exposed (011) facets for LTO and (001) facets for rutile TiO_2 in RLTO composite provide efficient lithium diffusion channels. The above mentioned advantages guarantee the excellent electrochemical performance of RLTO electrode with a reversible specific capacity of 142.9 mAh g^{-1} and 92.3% retention of its initial capacity at a rate of 30 C over 3000 cycles. The competitive rate capability matches well with the high surface area N-CNTs even at high current density, and an ideal electrochemical performance is realized with the superb energy density of 74.85 Wh kg^{-1} at a power density of 300 W kg^{-1} . Nevertheless, further optimization will be done to improve the energy density of the device.

Acknowledgements

Financial support from the 973 Program of China (2014CB643506, 2013CB922104) and the Director Fund of the Wuhan National Laboratory for Optoelectronics is gratefully acknowledged. The authors thank the Analytical and Testing Center of Huazhong University of Science & Technology and the Center of Micro-Fabrication and Characterization (CMFC) of WNLO for the measurements of the samples.

Note and references

- V. Aravindan, J. Gnanaraj, Y. Lee and S. Madhavi, *Chem. Rev.*, 2014, **114**, 11619.
- K. Naoi, W. Naoi, S. Aoyagi, J. Miyamoto and T. Kamino. *Acc. Chem. Res.*, 2013, **46**, 1075.
- X. Hu, Z. Deng, J. Suo and Z. Pan, *J. Power Sources*, 2009, **187**, 635.
- X. Wang and G. Shen, *Nano Energy*, 2015, **15**, 104.
- F. Zhang, T. Zhang, X. Yang, L. Zhang, K. Leng, Y. Huang and Y. Chen, *Energy Environ. Sci.*, 2013, **6**, 1623.
- Q. Wang, Z. Wen and J. Li, *Adv. Funct. Mater.*, 2006, **16**, 2141.
- H. Wang, Z. Xu, Z. Li, K. Cui, J. Ding, A. Kohandehghan, X. Tan, B. Zehri, B. Olsen, C. Holt and D. Mitlin, *Nano Lett.*, 2014, **14**, 1987.
- R. Wang, J. Lang, P. Zhang, Z. Lin and X. Yan, *Adv. Funct. Mater.*, 2015, **25**, 2270.
- R. Yi, S. Chen, J. Song, M. Gordin, A. Manivannan and D. Wang, *Adv. Funct. Mater.* 2014, **24**, 7433.
- H. Wang, C. Guan, X. Wang and H. Fan, *Small*, 2015, **11**, 1470.
- Z. Chen, Y. Yuan, H. Zhou, X. Wang, Z. Gan, F. Wang and Y. Lu. *Adv. Mater.*, 2014, **26**, 339.
- H. Kim, K. Park, M. Cho, M. Kim, J. Hong, S. Jung, K. Roh and K. Kang, *ChemElectroChem*, 2014, **1**, 125.
- H. Choi, J. Im, T. Kim, J. Park and C. Park, *J. Mater. Chem.*, 2012, **22**, 16986.
- K. Naoi, S. Ishimoto, Y. Isobe and S. Aoyagi, *J. Power Sources*, 2010, **195**, 6250.

15. H. Jung, N. Venugopal, B. Scrosati and Y. Sun, *J. Power Sources*, 2013, **221**, 266.
16. Y. Cai, B. Zhao, J. Wang and Z. Shao, *J. Power Sources*, 2014, **253**, 80.
17. H. Jung, S. Myung, C. Yoon, S. Son, K. Oh, K. Amine, B. Scrosati and Y. Sun, *Energy Environ. Sci.*, 2011, **4**, 1345.
18. H. Jung, M. Jang, J. Hassoun, Y. Sun and B. Scrosati, *Nat. Commun.*, 2011, **2**, 516.
19. W. Zuo, C. Wang, Y. Li and J. Liu, *Sci. Rep.*, 2015, **5**, 7780.
20. H. Xu, X. Hu, Y. Sun, W. Luo, C. Chen, Y. Liu and Y. Huang, *Nano Energy*, 2014, **10**, 163.
21. H. Choi, TaeHoon Kim, J. Im and C. Park, *Nanotechnology*, 2011, **22**, 405402.
22. L. Shen, E. Uchaker, X. Zhang and G. Cao, *Adv. Mater.*, 2012, **24**, 6502.
23. J. Liu, K. Song, P. Aken, J. Maier, Y. Yu, *Nano Lett.*, 2014, **14**, 2597.
24. G. Xu, B. Ding, P. Nie, L. Shen, J. Wang, X. Zhang, *Chem. Eur. J.*, 2013, **19**, 12306.
25. L. Gao, H. Hu, G. Li, Q. Zhu and Y. Yu, *Nanoscale*, 2014, **6**, 6463.
26. L. Gao, S. Li, D. Huang, Y. Shen and M. Wang, *J. Mater. Chem. A*, 2015, **3**, 10107.
27. Y. Wang, L. Gu, Y. Guo, H. Li, X. He, S. Tsukimoto, Y. Ikuhara and L. Wan, *J. Am. Chem. Soc.*, 2012, **134**, 7874.
28. Y. Xiong, Y. Xi, X. Li, Z. Li, *Carbon*, 2004, **42**, 1447.
29. Z. Wang, X. Xiong, L. Qie and Y. Huang, *Electrochim. Acta*, 2013, **106**, 320.
30. Q. Liu, Z. Pu, C. Tang, A. Asiri, A. Qusti, A. Youbi and X. Sun, *Electrochem. Commun.*, 2013, **36**, 57.
31. L. Chen, X. Zhang, H. Liang, M. Kong, Q. Guan, P. Chen, Z. Wu and S. Yu, *ACS Nano*, 2012, **6**, 7092.
32. L. Gao, X. Li, H. Hu, G. Li, H. Liu and Y. Yu, *Electrochim Acta*, 2014, **120**, 231.
33. Y. Jiang, K. Wang, X. Wu, H. Zhang and B. Bartlett, J. Chen, *ACS Appl. Mater. Interfaces*, 2014, **6**, 19791.
34. J. Chen and X. Lou, *Chem. Sci.*, 2011, **2**, 2219.
35. F. Wu, X. Li, Z. Wang and H. Guo, *Nanoscale*, 2013, **5**, 6936-6943.
36. X. Wang, D. Liu, Q. Weng, J. Liu, Q. Liang and C. Zhang, *NPG Asia Mater.*, 2015, **7**, e171.
37. Y. Lei, Z. Huang, Y. Yang, W. Shen, Y. Zheng, H. Sun and F. Kang, *Sci. Rep.*, 2013, **3**, 2477.
38. M. Wang, L. Qi, F. Zhao and S. Dong, *J. Power Sources*, 2005, **139**, 223.
39. M. Wang and S. Dong, *J. Power Sources*, 2007, **170**, 425.
40. M. Wang, F. Zhao and S. Dong, *J. Phys. Chem. B*, 2004, **108**, 1365.
41. S. Yang, S. Nam, T. Kim, J. Im, H. Jung, J. Kang, S. Wi, B. Park and C. Park, *J. Am. Chem. Soc.*, 2013, **135**, 7394.
42. L. Gao, R. Liu, H. Hu, G. Li and Y. Yu, *Nanotechnology*, 2014, **25**, 175402.
43. X. Jia, Y. Kan, X. Zhu, G. Ning, Y. Lu and F. Wei, *Nano Energy*, 2014, **10**, 344.
44. L. Yu, H. Wu and X. Lou, *Adv. Mater.*, 2013, **25**, 2296.
45. C. Lin, X. Fan, Y. Xin, F. Cheng, M. Lai, H. Zhou and L. Lu, *Nanoscale*, 2014, **6**, 6651.
46. J. Cheng, R. Che, C. Liang, J. Liu, M. Wang and J. Xu, *Nano Research*, 2014, **7**, 1043.
47. M. Rahman, J. Wang, M. Hassan, D. Wexler and H. Liu, *Adv. Energy Mater.*, 2011, **1**, 212.
48. Y. Shi, J. Gao, H. Abruña, H. Liu, H. Li, J. Wang and Y. Wu, *Nano Energy*, 2014, **8**, 297.
49. J. Choi, W. Ryu, K. Park, J. Jo, S. Jo, D. Lim and I. Kim, *Sci. Rep.*, 2014, **4**, 7334.
50. X. Li and J. Mao, *New J. Chem.*, 2015, **39**, 4430
51. H. Kim, M. Cho, M. Kim, K. Park, H. Gwon, Y. Lee, K. Roh, K. Kang, *Adv. Energy Mater.*, 2013, **3**, 1500.
52. A. Banerjee, K. Upadhyay, D. Puthusseri, V. Aravindan, S. Madhavi, S. Ogale, *Nanoscale*, 2014, **6**, 4387.